npj computational materials

www.nature.com/npjcompumats

ARTICLE OPEN

Check for updates

Intrinsic hard magnetism and thermal stability of a $ThMn_{12}$-type permanent magnet

Tumentsereg Ochirkhuyag[1], Soon Cheol Hong[2]✉ and Dorj Odkhuu[1]✉

Herein, we theoretically demonstrate that simple metal (Ga and Al) substitutional atoms, rather than the conventional transition metal substitutional elements, not only stabilize the $ThMn_{12}$-type $SmFe_{12}$ and $Sm(Fe,Co)_{12}$ phases thermodynamically but also further improve their intrinsic magnetic properties such that they are superior to those of the widely investigated $SmFe_{11}Ti$ and $Sm(Fe,Co)_{11}Ti$ magnets, and even to the state-of-the-art permanent magnet $Nd_2Fe_{14}B$. More specifically, the quaternary $Sm(Fe,Co,Al)_{12}$ phase has the highest uniaxial magnetocrystalline anisotropy (MCA) of about 8 MJ m^{-3}, anisotropy field of 18.2 T, and hardness parameter of 2.8 at room temperature and a Curie temperature of 764 K. Simultaneously, the Al and Ga substitutional atoms improve the single-domain size of the $Sm(Fe,Co)_{12}$ grains by nearly a factor of two. Numerical results of MCA and MCA-driven hard magnetic properties can be described by the strong spin-orbit coupling and orbital angular momentum of the Sm 4*f*-electron orbitals.

npj Computational Materials (2022)8:193 ; https://doi.org/10.1038/s41524-022-00821-8

INTRODUCTION

$ThMn_{12}$-type $SmFe_{12}$ alloy is known for its attractive intrinsic hard magnetic properties[1–8], which make it a potential high-performance permanent magnet. Despite its high saturation magnetization M_s and strong *uniaxial* magnetocrystalline anisotropy (MCA) K_u, obtaining a single-crystalline phase of the $ThMn_{12}$ structure is extremely difficult[9–13]. In particular, thermodynamically stable large (bulk)-scale production of $SmFe_{12}$ single crystals is in high demand for industrial applications such as electric motors and generators. To stabilize the $ThMn_{12}$ structure, a third substitutional metal element, including Ti or V[14–21], is essential. However, inclusions of these early transition metal (TM) elements are severely detrimental to intrinsic magnetic properties. For example, $SmFe_{11}Ti$ and $SmFe_{11}V$ ($SmFe_{10}V_2$) exhibit $\mu_0 M_s$ of 1.14−1.16 and 1.12 (0.81) T and K_u of 3.9−4.8 and 1.92 (1.58) MJ m^{-3} at room temperature[15–17,21], respectively, which are much lower than the corresponding values (1.64 T and 5.4−5.67 MJ m^{-3}) of the parent $SmFe_{12}$[22,23]. In contrast, the replacement of 20 at.% Fe at the 8f site with Co enhances $\mu_0 M_s$ up to 1.78 T and K_u up to 6.2 MJ m^{-3} at room temperature[22–24]. These findings, in addition to the enhanced Curie temperature ($T_c = 859$ K), make ternary $Sm(Fe_{0.8}Co_{0.2})_{12}$ superior to the state-of-the-art permanent magnet $Nd_2Fe_{14}B$ ($\mu_0 M_s = 1.57$ T, $K_u = 4.5$ MJ m^{-3}, and $T_c = 585$ K)[25–27]. However, the $ThMn_{12}$ structure of this ternary compound could only be synthesized with a limited film thickness of no more than 0.5 μm[22,23]. In addition to the structural instability, to maximize the permanent hard magnetic properties, the grain size of $SmFe_{12}$-based magnets must be prepared close to the single-domain (SD) size (~51−54 nm)[28,29]. However, preparing nanometre-sized $ThMn_{12}$-type $SmFe_{12}$ in a practical sample is quite difficult, which must be resolved to fully utilize $SmFe_{12}$ as a practical high-performance permanent magnet. The development of thermodynamically stable bulk-scale $SmFe_{12}$ single crystals with improved SD grain sizes and desirable intrinsic magnetic properties is thus essential and of timely importance.

In this paper, we propose a possible solution to realize an otherwise unstable $ThMn_{12}$-type $SmFe_{12}$ permanent magnet through systematic first-principles density functional theory (DFT), density functional perturbation theory (DFPT), and Monte Carlo (MC) simulations on ternary $Sm(Fe,M)_{12}$ and quaternary $Sm(Fe,Co,M)_{12}$ alloys (M is a 3*d* or 3*p* metal substitutional atom). In contrast to conventional TM substitutional elements, simple metal (SM) Al and Ga substitutional atoms stabilize the $ThMn_{12}$-type $Sm(Fe,Co)_{12}$ structure thermodynamically with an improved SD grain size and simultaneously enhanced K_u. We further predict that intrinsic hard magnetic properties at an elevated temperature of the proposed quaternary $Sm(Fe,Co,Al)_{12}$ and $Sm(Fe,Co,Ga)_{12}$ compounds in the present study are superior to those of the widely investigated $SmFe_{11}Ti$ and $Sm(Fe,Co)_{11}Ti$ compounds, and even to the present and reported values by the experimental[25–27] and previous theoretical studies[30,31] for the state-of-the-art permanent magnet $Nd_2Fe_{14}B$, including a higher T_c. We attribute the physical origin of the large MCA and MCA-driven hard magnetic properties to the strong spin-orbit coupling (SOC) and orbital angular momentum of the Sm 4*f*-electron shells.

RESULTS

Structural stability

We first inspected the structural stability of $ThMn_{12}$-type $SmFe_{12}$ structure upon M (M = Ti − Ga and Al) replacement. The formation enthalpy is defined as $H_f = (E_0 - \sum_i \mu_i N_i) N_A / N$, where E_0 is the total energy of the system and μ_i and N_i are the chemical potential and the number of decomposable component *i*, respectively. N_A is the Avogadro number and N is the total number of atoms in the computed unit cell. Our computed unit cell is composed of 2 Sm atoms at the 2a site and 24 Fe atoms at the inequivalent crystallographic 8f, 8i, and 8j sites (Wyckoff positions). Their optimized atomic coordinates along with the lattice parameters *a*, *b*, and *c* of $SmFe_{12}$ are given in Table 1. The present $a = b$ and *c* values are 8.481 and 4.661 Å, respectively, in agreement with the

[1]Department of Physics, Incheon National University, Incheon 22012, South Korea. [2]Department of Physics, University of Ulsan, Ulsan 44610, South Korea.
✉email: schong@ulsan.ac.kr; odkhuu@inu.ac.kr

experimental (8.44 and 4.81 Å)[5,22] and previous theoretical results (8.46−8.49 and 4.68−4.81 Å)[8,32]. Correspondingly, the three different substitution sites of M atoms for $SmFe_{12-x}M_x$ (x = 0.5, 1, and 2) were considered and denoted as M(8f), M(8i), and M(8j). For each configuration, from the total energy minimization, the M atoms were identified to prefer a uniform distribution[24], as indicated in Fig. 1a–c. The optimized lattice parameters of $SmFe_{10}M_2$ with the preferred M site are listed in Table 2. In agreement with an experiment[33], $ThMn_{12}$-type $SmFe_{12}$ is not a stable phase and decomposes into bulk-Sm and *α*-Fe phases, as expected from the calculated positive H_f values of 2.9 kJ mol^{-1} from the standard DFT and 6.5 kJ mol^{-1} from the DFT plus U (DFT + U) with U_{eff} = 6 eV. A slightly smaller value of H_f = 1.8 kJ mol^{-1} was reported in the previous DFT calculations[34]. Nevertheless, the single-crystalline $ThMn_{12}$ phase can be obtained in $SmFe_{11}Ti$ form[15–17]. For a ternary system, simply considering decomposition into the final constituent elements is not sufficient for predicting the structural stability[35–38]. The most competitive binary decomposable phases for Sm−Fe−M are identified by constructing the convex hull phase diagram[35–38].

We show heat map of the calculated formation enthalpy of the ternary Sm−Fe−Ti system in Fig. 2a. The solid nodes on the phase diagram represent the present ternary $SmFe_{12-x}Ti_x$ phases (x = 0.5, 1, and 2), while the known binary and elemental phases are indicated by the open nodes. In the Sm−Fe−Ti diagram, since all Sm−Fe binary phases are unstable against their elemental bulk-Sm and *α*-Fe phases, we have chosen the bulk-Sm and *α*-Fe as decomposable phases rather than a Sm−Fe binary phase. We find that the H_f values of the known binary Sm_2Fe_{17}, Sm_3Fe_{29}, Sm_6Fe_{23}, and $SmFe_2$ phases are 8.4, 9.2, 4.9, and 0.9 kJ mol^{-1}, respectively. In the Ti-poor region (i.e., x = 0.5), Fe_2Ti is chosen as the decomposable binary phase for Sm−Fe−Ti, as indicated by the dotted lines in Fig. 2a. In the Ti-rich region (i.e., x = 1 and 2), Fe_2Ti + FeTi decomposition is taken into account (solid lines). The numerical values of the obtained H_f^{elm} (against the elemental decomposition) and H_f^{bin} (against the binary decomposition) of $SmFe_{12-x}Ti_x$ phases are shown in Fig. 2b for x = 0, 0.5, 1, and 2. Both H_f^{elm} and H_f^{bin} decrease as x increases and reach the negative values of −10.7 and −4.2 kJ mol^{-1} at x = 2, respectively. For $SmFe_{11}Ti$, H_f^{elm} = −2.6 kJ mol^{-1} and H_f^{bin} = 0.2 kJ mol^{-1}. Since the single-crystalline $SmFe_{11}Ti$ phase is practically achieved in the bulk form[15–17], the latter value (0.2 kJ mol^{-1}) of $SmFe_{11}Ti$ is referred to as a threshold of the $ThMn_{12}$-phase stability in the present study. The aforementioned experimental observations of the reduced $\mu_0 M_s$ and K_u upon the Ti substitution[15–17] have also been obtained

Table 1. Optimized lattice parameters *a*, *b*, and *c* (Å), and angles *α*, *β*, and *γ* (°), and internal atomic coordinates of $ThMn_{12}$-type $SmFe_{12}$.

Lattice parameter		*a*	*b*	*c*	*α*	*β*	*γ*
$SmFe_{12}$		8.481	8.481	4.661	90	90	90
Element	Wyckoff letter	Atomic coordinate					
Sm	2a	(0, 0, 0), (1/2, 1/2, 1/2)					
Fe	8f	(±1/4, ±1/4, 1/4), (±1/4, ±1/4, 3/4)					
Fe	8i	(0 ± *x*, 1/2, 1/2), (0, 1/2 ± *x*, 0), (1/2 ± *x*, 0, 0), (1/2, 0 ± *x*, 1/2)					
Fe	8j	(0 ± *y*, 0, 1/2), (0, 0 ± *y*, 1/2), (1/2 ± *y*, 1/2, 0), (1/2, 1/2 ± *y*, 0)					

x = 0.14, *y* = 0.23.

Table 2. Optimized lattice parameters *a*, *b*, and *c* (Å), and spin magnetic moment μ_S (μ_B per atom) of the different atom types in $SmFe_{10}M_2$ for M = Ti-Ga and Al.

	a = *b*	*c*	μ_S				
			Sm	Fe(8f)	Fe(8i)	Fe(8j)	M
Ti	8.522	4.729	−5.48	1.68	2.14	2.03	−0.62
V	8.518	4.721	−5.47	1.71	1.98	2.03	−1.01
Cr	8.415	4.667	−5.45	1.68	2.12	2.04	−1.72
Mn	8.431	4.640	−5.44	1.65	2.17	2.00	−2.39
Fe	8.481	4.661	−5.44	1.78	2.53	2.34	
Co	8.488	4.672	−5.30	2.18	2.58	2.50	1.52
Ni	8.467	4.678	−5.44	2.10	2.57	2.39	0.69
Cu	8.515	4.697	−5.46	2.09	2.54	2.36	0.11
Zn	8.562	4.708	−5.49	1.96	2.50	2.31	−0.08
Ga	8.574	4.739	−5.49	1.88	2.47	2.25	−0.09
Al	8.515	4.718	−5.47	1.74	2.38	2.18	−0.10

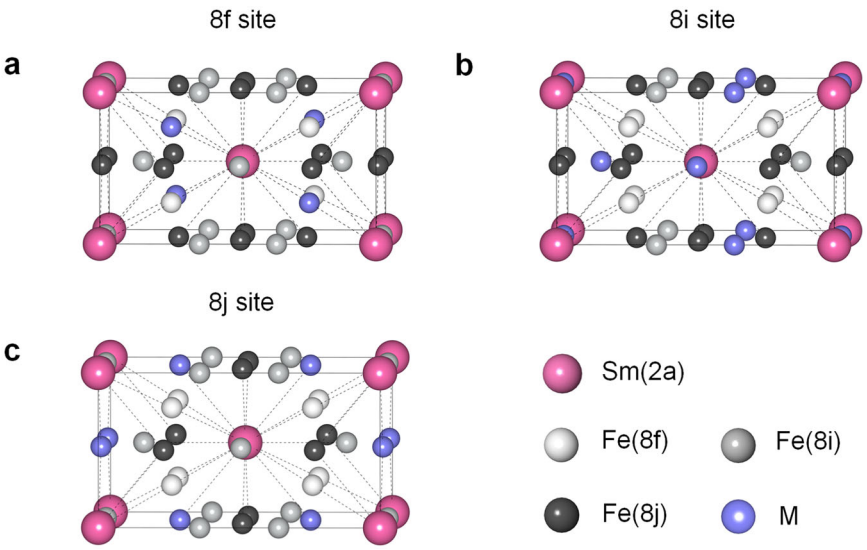

Fig. 1 Atomic structures used for calculations. $ThMn_{12}$-type atomic structures of $SmFe_{12-x}M_x$ (when x = 2) for the **a** 8f, **b** 8i, and **c** 8j site M substitutes. Only the most stable configuration of the distribution patterns of the M atoms is shown for each substitution site.

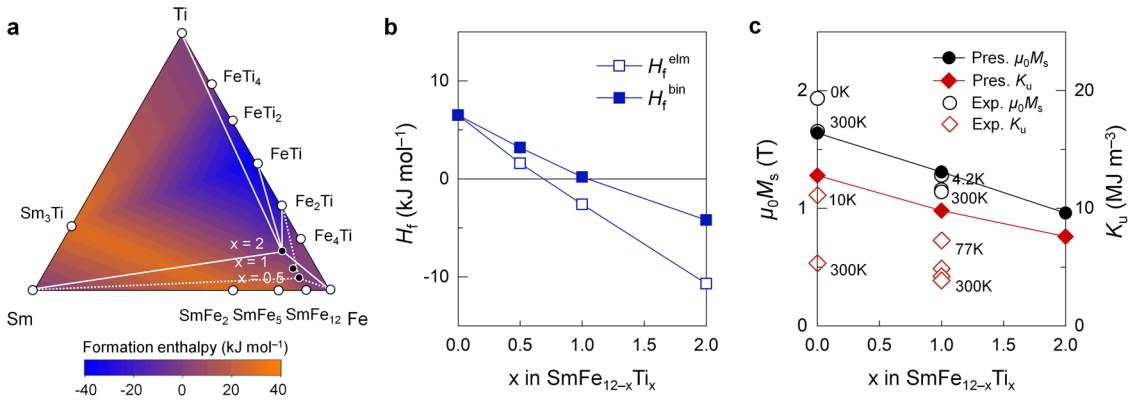

Fig. 2 Structural stability and intrinsic magnetic properties of Sm−Fe−Ti system. a Heat map of the formation enthalpy of the ternary Sm−Fe−Ti system. Open nodes mark the known elemental and binary phases. Solid nodes represent the present ternary $SmFe_{12-x}M_x$ (x = 0.5, 1, and 2) phases. Dotted and solid lines are the projections of the convex hull construction into compositional space. **b** Formation enthalpy H_f and **c** saturation magnetization $\mu_0 M_s$ (left) and uniaxial magnetocrystalline anisotropy K_u (right) of $SmFe_{12-x}M_x$ (x = 0, 0.5, 1, and 2). The corresponding experimental results for $SmFe_{12}$ measured at 0−300 K[22,23] and $SmFe_{11}Ti$ at 4.2−300 K[15–17] are indicated by the open symbols, where the result at 0 K is determined by fitting with low-temperature measurements[22].

in our calculations, as shown in Fig. 2c, which will be discussed more explicitly in the following paragraphs.

Figure 3a presents the H_f^{bin} values of $SmFe_{12-x}M_x$ (M = Ti − Ga and Al; x = 0.5 and 2) for M(8f), M(8i), and M(8j). Early TMs, Ti to Mn, prefer the 8i site rather than the 8f and 8j sites for both x = 0.5 and 2. A similar trend is also observed for $SmFe_{11}M$, which, except for $SmFe_{11}Ti$, is not shown for simplification of the figure. Hereafter, we thus refer to the results corresponding to the practically acceptable stoichiometry $SmFe_{10}M_2$, unless specifically mentioned. These results are supported by the experiment in which Ti and V dopants occupied the 8i site[39]. Late TMs, except for Co(8f), prefer the 8j site. The different site preferences can be interpreted in correlation with the atomic radii and electronegativity. In the $SmFe_{12}$ structure, the 8i site (3.06 and 4.98 Å) is farther from Sm than the 8j (3.04 and 4.82 Å) and 8f (3.21 and 3.21 Å) sites (Table 1). Ti − Mn with large atomic radii thus naturally prefer the 8i site. In contrast, Ni − Ga attract Sm more than Ti − Mn, as Ni − Ga (1.65−1.91) have higher electronegativities than Ti − Mn (1.54−1.66).

As predicted from the H_f^{bin} values (Fig. 3a), the Ga (H_f^{bin} = −1.5 kJ mol^{-1}) and Al (−3.1 kJ mol^{-1}) substitutional atoms stabilize the $ThMn_{12}$ structure. These SMs improve the stability comparably to the conventional stabilizing early TM substitutional elements Ti (−4.2 kJ mol^{-1}) and V (0.2 kJ mol^{-1}). On the other hand, the dopant amount of x = 0.5 is not sufficient for stabilizing the $ThMn_{12}$ phase as the aforementioned basic requirement of the crystal formation (H_f^{bin} < 0.2 kJ mol^{-1}; as indicated by the horizontal dashed line in Fig. 3a) is not fulfilled. Practically, $SmFe_{12-x}Ti_x$ and $SmFe_{12-x}V_x$ phases are synthesized with a nearly perfect $ThMn_{12}$ structure when x ≥ 1[14–17,20,21]. Furthermore, a very recent experiment reported that the stability of $SmFe_{8.8}Co_{2.2}Ti$ was greatly improved by Ga addition[33]. The authors also predicted theoretically that Ga is the most effective stabilizing elements with higher $\mu_0 M_s$ over Ti, V, and Cr dopants. Our prediction in support with these experimental and theoretical studies suggests a possible synthesis of the single-crystalline $ThMn_{12}$ structure, including a series of $Sm(Fe,Co)_{12}$ and $Sm(Fe,Co,Ti)_{12}$ compounds, with Al and/or Ga, at least at a low temperature.

Intrinsic magnetic properties

The Slater − Pauling-like behavior of $\mu_0 M_s$ is evident in Fig. 3b for the late TMs (Mn − Zn). For each M, only the result obtained by the full-potential calculations for the preferred substitution site is presented. For $SmFe_{12}$, the experimental $\mu_0 M_s$ of 1.94 T at 0 K determined by fitting with low-temperature measurements[22] is underestimated in the present theory (1.64 T). This discrepancy might be attributed to the existence of the *α*-Fe phase and surface/interface effect in a real thin-film sample, which are fully ignored in the present simulation. To obtain microscopic insight, we decompose $\mu_0 M_s$ into the atomic-level spin magnetic moment (μ_S) in Table 2. The spin moment contributions of the Fe(8f), Fe(8i), and Fe(8j) atoms to $\mu_0 M_s$ are 1.78, 2.53, and 2.34 μ_B, respectively. The Sm 4*f* spin moment (−5.44 μ_B) is antiparallel to the Fe 3*d* spin moment, which is mediated by the Sm 5*d* orbitals[40,41]. The magnitude of μ_S adheres to the high-spin state. Nevertheless, the orbital moment contribution (μ_L = 2.25 μ_B) of the 4*f* electrons of Sm (antiparallel to its spin moment according to the 3rd Hund's rule, thus parallel to the Fe 3*d* spin moment) to $\mu_0 M_s$ is substantial, whereas those from the Fe 3*d* orbitals are <0.1 μ_B.

In the Λ-shape curve (Slater − Pauling-like) shown in Fig. 3b, a peak occurs for M = Co; $\mu_0 M_s$ increases from 1.64 T for $SmFe_{12}$ to 1.68 T for $SmFe_{10}Co_2$. A similar trend was found in the room-temperature measurement[22], as indicated by the circle symbols in Fig. 3b; 1.78 T for $SmFe_{9.6}Co_{2.4}$ and 1.64 T for $SmFe_{12}$. But this is not the case in the extrapolated zero-temperature measurement[22]; $\mu_0 M_s$ decreases from 1.94 T for $SmFe_{12}$ to 1.88 T for $SmFe_{9.6}Co_{2.4}$. The difference could be attributable to the aforementioned shortcomings as well as to dissimilar Co concentrations in the present theory (i.e., $SmFe_{10}Co_2$) and experiment (i.e., $SmFe_{9.6}Co_{2.4}$)[22]. Both the theory and experiment reveal that the early TMs (Ti − Mn) greatly lower $\mu_0 M_s$ (0.75 − 0.95 T)[16,17,21] because of their antiparallel spin coupling to Fe (Table 2). Thus, the concentration of these early TMs should be kept at a minimal. For $SmFe_{11}Ti$, the present $\mu_0 M_s$ is 1.31 T, which is comparable with 1.28−1.14 T at 4.2−300 K in the experiments[15–17]. In contrast to the early TMs, the nonmagnetic late TMs and SMs are not as detrimental to $\mu_0 M_s$ (1.2−1.3 T). Overall, $\mu_0 M_s$ is mainly affected by the magnetic moments of the M atom and its neighboring Fe atoms, as addressed explicitly in Table 2.

Figure 3c shows the computed K_u of $SmFe_{10}M_2$ (M = Ti − Ga and Al). We recall from ref. [24] that the K_u values of $SmFe_{12}$ are 12.8 MJ m^{-3} in the DFT calculation and 10.6 MJ m^{-3} in the DFT + U calculation (with U_{eff} = 6 eV). Both values are in reasonable agreement with the low-temperature experimental values of 10.76−11.1 MJ m^{-3} at 100−10 K[23]. The K_u results thus refer to those from DFT calculations without the U_{eff} parameter to minimize computational complications. From a theoretical point of view, we here would like to remind that direct comparison with experiment, particularly on the precise magnitude of MCA, requires some caution, as an accurate treatment of *f*-electron

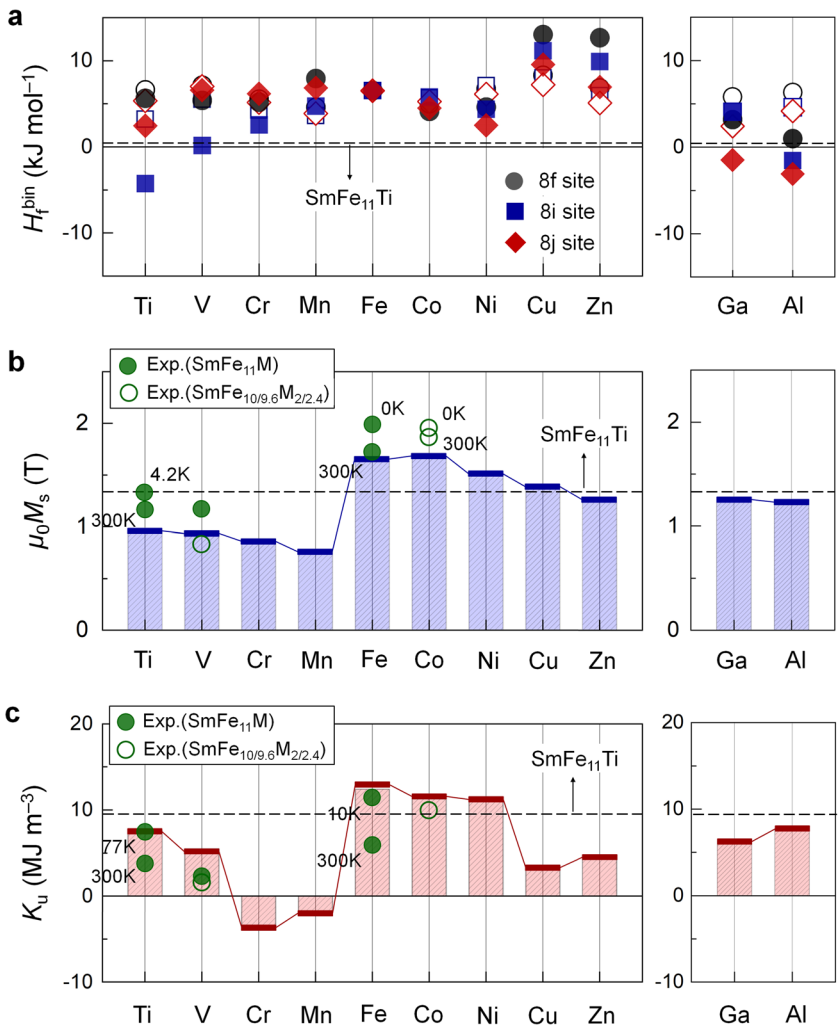

Fig. 3 Impact of single-element substitution on the stability and intrinsic magnetic properties at 0 K. a Formation enthalpy H_f^{bin} of $SmFe_{12-x}M_x$ with x = 0.5 (open) and 2 (solid symbols) for M = Ti–Zn (transition metals), Ga and Al (simple metals) for the 8f, 8i, and 8j sites. Horizontal dashed line corresponds to the calculated H_f^{bin} value of $SmFe_{11}Ti$, a threshold of the $ThMn_{12}$-phase stability. **b** Saturation magnetization $\mu_0 M_s$ and **c** uniaxial magnetocrystalline anisotropy K_u of $SmFe_{10}M_2$ with the preferred M site. Solid and open circles indicate the experimental data for $SmFe_{11}M$ and $SmFe_{10}V_2$/$SmFe_{9.6}Co_{2.4}$ measured at 0–300 K[14–17,20–23], respectively, where the result at 0 K is determined by fitting with low-temperature measurements[22].

systems by first-principles is quite challenging. Nevertheless, our theory for M = Co (K_u = 11.2 MJ m^{-3}) further supports the low-temperature experiment in which the substitution of Co atoms for 20 at.% Fe at the 8f site reduced K_u to 9.73 MJ m^{-3} at 10 K[23]. According to Fig. 3c, substantial reductions obviously appear for the other TM substitutions, including the reference $SmFe_{11}Ti$ system (K_u = 9.8 MJ m^{-3}). Similar reductions were also observed for $SmFe_{11}Ti$ (7.2–3.9 MJ m^{-3} at 77–300 K)[15–17] and $SmFe_{10}V_2$ (1.58 MJ m^{-3} at 300 K) in the experiments[21]. Cr and Mn even turn the magnetic easy axis from the *c* axis to the *ab* plane (which is improper for permanent magnets). In contrast, the SM substitutes (Ga and Al), which stabilize the $ThMn_{12}$ structure, still preserve the MCA uniaxiality. In particular, K_u reaches as high as 7.6 MJ m^{-3} for M = Al, which is 6.3 MJ m^{-3} for M = Ga. Hence, in the discussion below we focus mainly on Al rather than Ga. Note that this uniaxial MCA makes $Sm(Fe,M)_{12}$-based magnets a potential high-performance permanent magnet beyond the other $ThMn_{12}$-type $Nd(Fe,M)_{12}$ magnets with a biaxial MCA[12,13,18,19].

Recalling the favorable formation (H_f^{bin} < 0 in Fig. 3a), in a real sample, Al (which has the smallest atomic radius among the M) could occupy either the 8j or 8i site, or both. These two sites are energetically competitive and differ in H_f^{bin} by only within 1.4 kJ mol^{-1}. For a given temperature, we estimate the occupation probability $\langle N_v \rangle$ of the Al substitution sites (*v* = 8f, 8i, and 8j) by using Maxwell-Boltzmann statistics. As shown in Fig. 4, the occupation probability of the Al substitute at the 8j (8i) site decreases (increases) with temperature; $\langle N_{8i} \rangle : \langle N_{8j} \rangle$ = 0.30 : 0.57 at 300 K and 0.33:0.48 at 500 K. A certain amount of the 8f site could also be occupied by the Al atoms in a high-temperature sample. We further find that K_u is almost independent of the stable 8i (10.9 MJ m^{-3}) and 8j (7.6 MJ m^{-3}) sites. From a practical viewpoint, this substitution-site-independent uniaxial feature of the MCA is worth noting, in addition to the abundance of Al on earth.

Impact of multielement substitution

We next explored the effects of multielement substitution on the intrinsic permanent magnetic properties. According to Fig. 3, only Co substitution maximizes $\mu_0 M_s$, while Ti, V, Ga, and Al improve the $SmFe_{12}$ stability. To support this scenario, we extended our calculations to the quaternary stoichiometries $SmFe_{10}CoM$ and $SmFe_9Co_2M$ (M = Ti, V, Ga, and Al). For each M, we considered

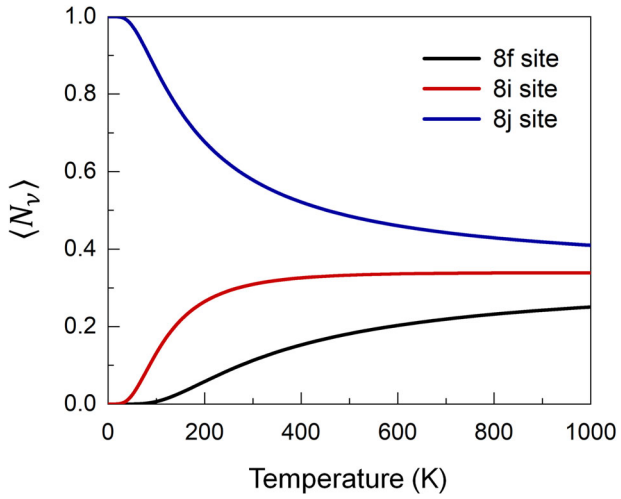

Fig. 4 Temperature-dependent occupation probability. Occupation probability $\langle N_v \rangle$ of the Al substitution sites (v = 8f, 8i, and 8j) at an elevated temperature in $SmFe_{10}Al_2$.

several different substitutional configurations of the M atoms while the Co atoms were kept fixed at their optimized 8f sites, as shown in Fig. 1a. As examples, we illustrate the most favorable structures of $SmFe_{10}CoAl$ and $SmFe_9Co_2Al$ compounds obtained from our total energy minimization in Fig. 5a and b, respectively.

Figures 5c, d and e show the H_f^{bin}, $\mu_0 M_s$, and K_u values, respectively, of $SmFe_{10}CoM$ and $SmFe_9Co_2M$ for M = Ti, V, Ga, and Al. Here, the formation enthalpy H_f^{bin} is calculated against $Fe_3Co + Fe_3M + FeCo + FeM$ decomposition. All the quaternary phases considered here, except for M = V, are stable as their H_f^{bin} values are <0.2 kJ mol^{-1} for $SmFe_{11}Ti$. The obtained $\mu_0 M_s$ ranges from 1.3 T (M = Ti and V) to 1.45 T (M = Ga and Al), which are sufficient values for practical permanent magnet applications. In our further prediction, as shown in Fig. 5e, the main trend of the K_u of $SmFe_{10}M_2$ (Fig. 3c) is roughly preserved for both $SmFe_{10}CoM$ and $SmFe_9Co_2M$; K_u reaches the largest values of 12.5 MJ m^{-3} for $SmFe_9Co_2Al$ and 14.1 MJ m^{-3} for $SmFe_{10}CoAl$. We emphasize that the latter value is the highest K_u achieved in the present study, which is 1.3−4.3 MJ m^{-3} larger than those of $SmFe_{12}$ (12.8 MJ m^{-3}) and $SmFe_{11}Ti$ (9.8 MJ m^{-3}). More remarkably, these K_u values (12.5−14.1 MJ m^{-3}) are even superior to those obtained in the present (5.4 MJ m^{-3}) and previous theoretical (4.31 MJ m^{-3})[31] and experimental studies (4.5 MJ m^{-3})[27] for the state-of-the-art permanent magnet $Nd_2Fe_{14}B$.

Microscopic origin of magnetic anisotropy

The microscopic origin of MCA is the SOC interaction between the atomic orbital angular momentum (**L**) and the atomic spin angular momentum (**S**), given by $H_{SOC} = \lambda \mathbf{L} \cdot \mathbf{S}$, where λ is the atomic SOC parameter. We provide the atom-by-atom contributions to MCA energy (E_{MCA}) for the selected $SmFe_{12}$, $SmFe_{10}Co_2$, $SmFe_{10}CoAl$ and $SmFe_9Co_2Al$ compounds in Fig. 5f. Here, E_{MCA} is scaled down to the microscopic atomic level (meV atom^{-1}), rather than the macroscopic energy density (MJ m^{-3}). For $SmFe_{12}$ and $SmFe_{10}Co_2$, Sm dominates E_{MCA}, whereas the contributions from the Fe and Co 3*d* orbitals are 2 orders of magnitude smaller. The two equivalent Sm sites in the unit cells of $SmFe_{12}$ and $SmFe_{10}Co_2$ are no longer symmetrically equivalent in the quaternary compounds due to the presence of the 8j-site substitutional atoms. In the optimized structure, the 2 Sm atoms are also not equally separated from the Al(8j) sites. As described in Fig. 5a, the $Sm_1 - Al_1$ ($Sm_1 - Al_2$) and $Sm_2 - Al_1$ ($Sm_2 - Al_2$) separations are 3.08 (4.79) and 4.88 (3.11) Å, respectively. We find that the Sm_1 site predominantly contributes to the large E_{MCA} and that Sm_2 undermines E_{MCA}. The same trend holds for the orbital magnetic anisotropy ($\Delta\mu_L$) in Fig. 5g, defined as $\Delta\mu_L = (\mu_L)_c - (\mu_L)_a$, consistent with the Bruno theory[42]; $\Delta\mu_L$ is larger by 1 − 2 orders of magnitude in the Sm 4*f* orbitals than in the 3*d* orbitals. The contribution from the Al 3*p* orbitals to E_{MCA} ($\Delta\mu_L$) is essentially zero.

Thermodynamic phase stability

The Helmholtz free energy can be written as $F(T,V) = E_0(V) + F_{el}(T,V) + F_{vib}(T,V) + F_{mag}(T,V)$, where $E_0(V)$ is the zero-temperature total energy of the system, and $F_{el}(T,V)$, $F_{vib}(T,V)$, and $F_{mag}(T,V)$ are the electronic, vibrational, and magnon contributions of the free energy, respectively. The phase stability against phase decomposition into the most competitive decomposable compounds can be described thermodynamically by the change in the free energy[43,44]: $\Delta F(T,V) = F(T,V) - \sum_i N_i F_i(T,V)$, where N_i and $F_i(T,V)$ are the number and free energy of decomposable compounds *i*, respectively. The temperature-dependent free energy contributions of $F_{el}(T,V)$, $F_{vib}(T,V)$, and $F_{mag}(T,V)$ are shown in Fig. 6a for $SmFe_{12}$, $SmFe_{10}Co_2$, $SmFe_{10}CoAl$, and $SmFe_9Co_2Al$. In Fig. 6a, the same for $SmFe_{11}Ti$ is also shown as a reference. All systems exhibit similar trends in the free energy against temperature; $F_{el}(T,V)$ and $F_{vib}(T,V)$ decrease as temperature increases, whereas $F_{mag}(T,V)$ increases with temperature. Obviously, the former two contributions, particularly the vibrational, mainly determine the temperature-induced changes in the free energy.

Figure 6b shows the temperature-dependent free energy change $\Delta F(T,V)$ and its contributions, i.e., $\Delta F_{el}(T,V)$, $\Delta F_{vib}(T,V)$, and $\Delta F_{mag}(T,V)$, for $SmFe_{12}$, $SmFe_{11}Ti$, $SmFe_{10}Co_2$, $SmFe_{10}CoAl$, and $SmFe_9Co_2Al$. As a generic for all compounds, $\Delta F(T,V)$ decreases as temperature increases, which is almost entirely accounted for by the vibrational contribution. The other two contributions, $\Delta F_{el}(T,V)$ and $\Delta F_{mag}(T,V)$, are insignificant. For $SmFe_{12}$, $\Delta F(T,V)$ changes its sign from positive to negative at temperature around 1000 K. Similar results were reported in previous calculations although the sign change in $\Delta F(T,V)$ occurs much earlier around 200 K[34]. The main cause for this discrepancy is the choice of the exchange-correlation in the computation, as mentioned early; DFT + U in the present study and DFT in the previous study[34]. The Ti and Co substitutional atoms reduce the onset temperature significantly; around 200 K for $SmFe_{11}Ti$ and 500 K for $SmFe_{10}Co_2$. This indicates that $SmFe_{11}Ti$ is thermally stable as observed in the experiments[15–17]. For $SmFe_{10}CoAl$ and $SmFe_9Co_2Al$, $\Delta F(T,V)$ remains negative over the temperature range, which suggests an acceptable thermodynamic stability of $Sm(Fe,Co,Al)_{12}$ magnets under realistic conditions.

Exchange interaction

The exchange interaction in the Heisenberg model is calculated to determine the intrinsic hard magnetic properties at an elevated temperature. When an external magnetic field is not applied, the Heisenberg spin Hamiltonian is expressed as $H = -(1/2)\sum_{i \neq j} J_{ij} \mathbf{S}_i \cdot \mathbf{S}_j - K_u \sum_i (\mathbf{S}_i \cdot \mathbf{e})^2$, where J_{ij} is the exchange coupling interaction between two spins $\mathbf{S}_i$ (at the *i* site) and $\mathbf{S}_j$ (at the *j* site), and **e** is the unit vector along the magnetic easy axis. The exchange interaction parameters were estimated by the constrained local moment approach in the DFT calculations through $J_{ij} = (\Delta_{ij} - \Delta_i - \Delta_j)/4n_i z_{ij} S_i S_j$[45,46], where Δ_{ij} is the energy difference between the magnetic ground state and the excited state (i.e., the magnetic moments at sites *i* and *j* are inverted). Δ_i (Δ_j) refers to the inverted magnetic moment at the *i* (*j*) site. n_i is the number of atoms in sublattice *i*, and z_{ij} is the number of nearest neighbor sites in sublattice *j* relative to sublattice *i*. The exchange coupling integral J_{ex} is the sum of J_{ij}, i.e., $J_{ex} = \sum_{i,j} z_{ij} J_{ij}$. In this approach, the spin in the *i*th sublattice is assumed to interact with the *j*th neighbor only while the other possible intrasublattice

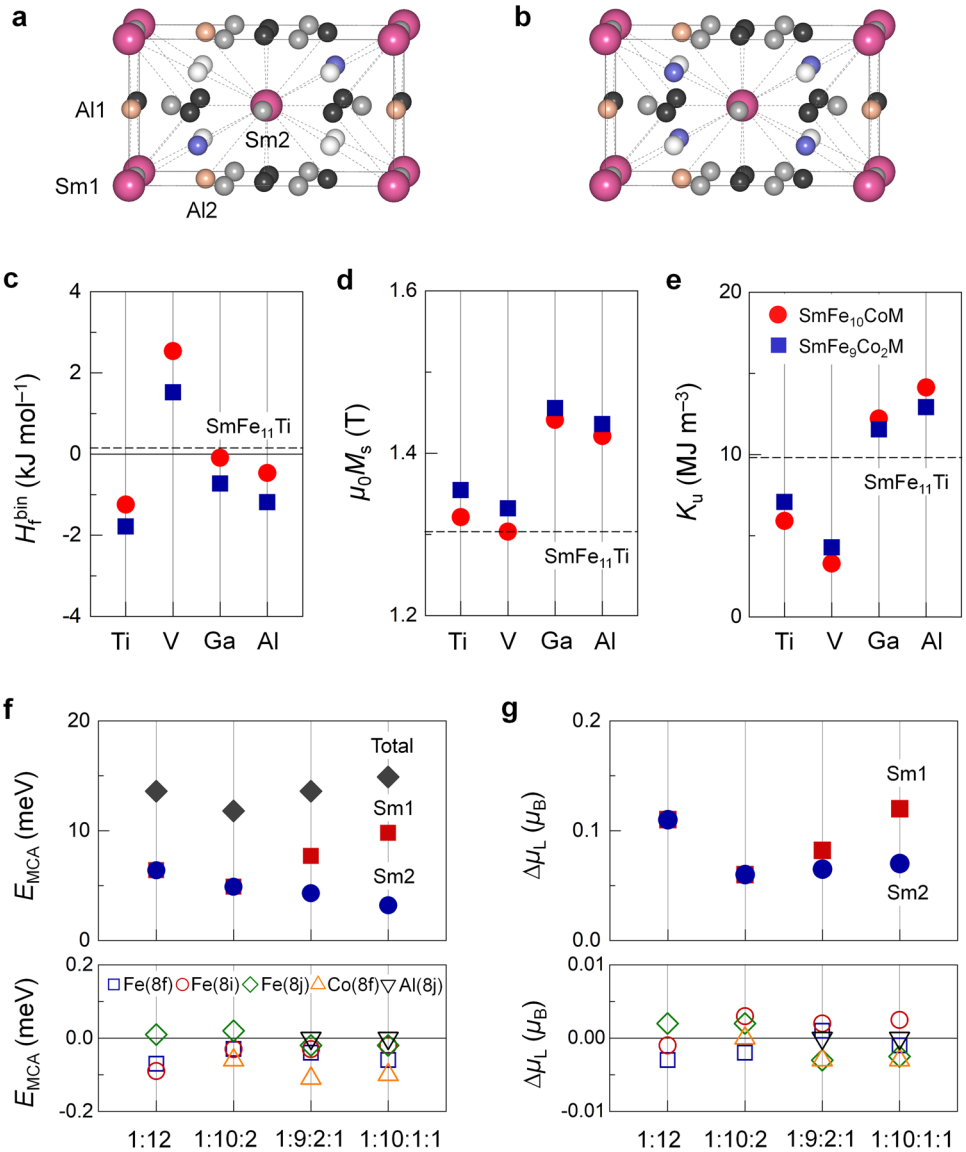

Fig. 5 Impact of multielement substitution on the stability and intrinsic magnetic properties at 0 K. Optimized atomic structures of **a** $SmFe_{10}CoAl$ and **b** $SmFe_9Co_2Al$. Blue and orange spheres represent the Co and Al substitutional atoms, respectively. Other atomic symbols are the same as those used in Fig. 1. **c** Formation enthalpy H_f^{bin}, **d** saturation magnetization $\mu_0 M_s$, and **e** uniaxial magnetocrystalline anisotropy K_u of $SmFe_{10}CoM$ and $SmFe_9Co_2M$ for M = Ti, V, Ga, and Al. Horizontal dashed lines correspond to the calculated results of $SmFe_{11}Ti$ for reference. **f** Atom-by-atom contribution to magnetocrystalline anisotropy energy E_{MCA} and **g** orbital magnetic anisotropy $\Delta\mu_L$ of $SmFe_{12}$ (denoted as 1:12), $SmFe_{10}Co_2$ (1:10:2), $SmFe_9Co_2Al$ (1:9:2:1), and $SmFe_{10}CoAl$ (1:10:1:1).

exchange interactions are disregarded. The present results of the exchange interaction parameters in the analyses below have to be thus double checked with a more precise state-of-the-art approach.

Figure 7a shows the calculated J_{ij} values for the different atomic couplings in $SmFe_{12}$, $SmFe_{11}Ti$, $SmFe_{10}Co_2$, $SmFe_{10}CoAl$, and $SmFe_9Co_2Al$. The positive (negative) exchange parameter reflects the preference for spin parallel (antiparallel) coupling between the two magnetic moments. To inspect the validity of our results, we first calculated the exchange interactions of the prototypical ferromagnetic systems, including α-Fe, α''-$Fe_{16}N_2$[47], and B2-FeCo[46]. For α-Fe, the nearest- and next-nearest-neighbor Fe−Fe interactions are 16.8 and 7.6 meV, respectively. These values are in good agreement with previous calculations[48,49]. The third-nearest-neighbor interactions are found to be rather small, although J_{ij} is a long-range interaction. As shown in Fig. 7a, the Fe−Fe exchange parameters are more or less retained in $SmFe_{12}$ and $SmFe_{11}Ti$, while the Sm−Fe interactions prefer antiparallel coupling. The Fe(8i)−Fe(8i) interaction is the strongest among the Fe−Fe interactions since the Fe(8i) atom has the largest spin magnetic moment compared to the other two sites (Table 2). In the Sm−Fe−Co and Sm−Fe−Co−Al systems, the Co substitute enhances all the first-nearest-neighbor exchange parameters, which indeed occurs quite often in Fe−Co magnetic systems[46,49]. The second-nearest-neighbor Fe−Fe and Sm−Fe interactions are not much altered from those of $SmFe_{12}$, and the Fe−Al interactions are negligible (thus not shown).

Temperature-dependent intrinsic magnetic properties

We plot the temperature-dependent $\mu_0 M_s$ and K_u obtained from the constrained MC simulation in Fig. 7b and c, respectively. In the MC simulation, we adopted an 8.47 nm × 8.47 nm × 4.64 nm cell with 26,000 atoms under periodic boundary conditions.

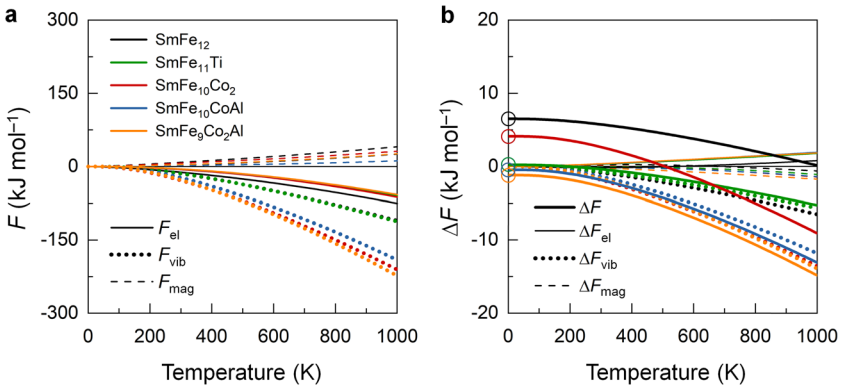

Fig. 6 Thermodynamic phase stability. Temperature-dependent **a** free energy contributions of the electronic $F_{el}(T, V)$, vibrational $F_{vib}(T, V)$, and magnon $F_{mag}(T, V)$, and **b** free energy change $\Delta F(T, V)$ of $SmFe_{12}$, $SmFe_{11}Ti$, $SmFe_{10}Co_2$, $SmFe_{10}CoAl$, and $SmFe_9Co_2Al$. In **b** the contributions of the electronic $\Delta F_{el}(T, V)$, vibrational $\Delta F_{vib}(T, V)$, and magnon $\Delta F_{mag}(T, V)$ to $\Delta F(T, V)$ are also presented for each compound. Open symbols at 0 K represent the formation enthalpy H_f^{bin}.

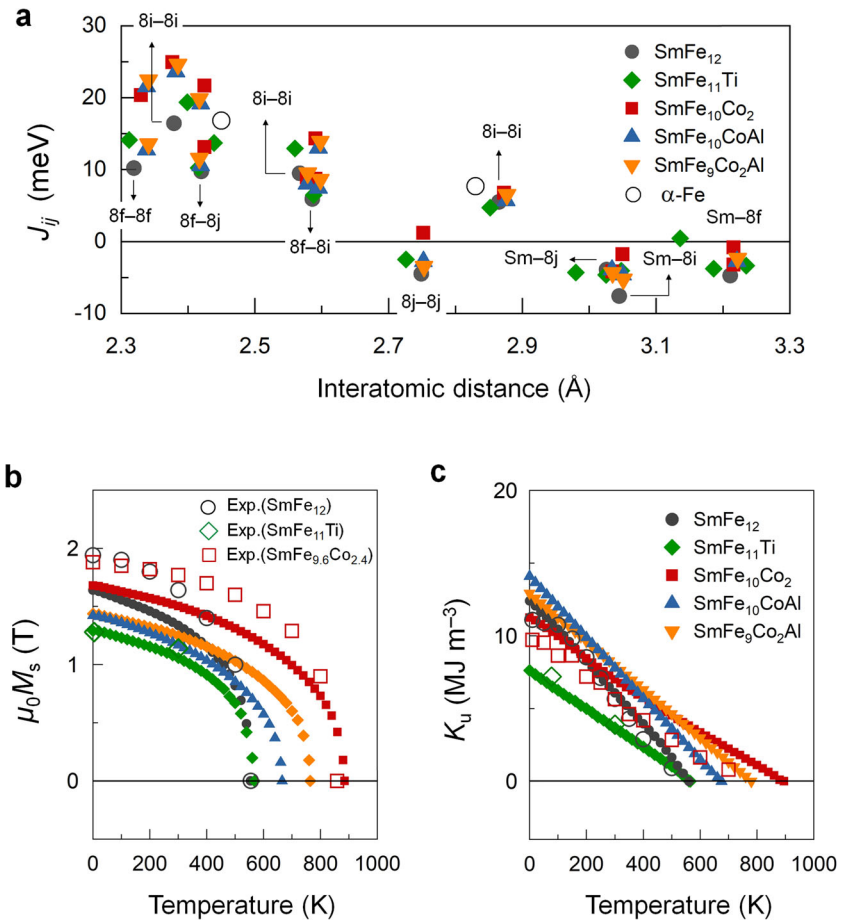

Fig. 7 Temperature-dependent intrinsic magnetic properties. a Exchange interaction parameters J_{ij} as a function of the interatomic distance, **b** saturation magnetization $\mu_0 M_s$ versus temperature, and **c** uniaxial magnetocrystalline anisotropy K_u versus temperature of $SmFe_{12}$, $SmFe_{11}Ti$, $SmFe_{10}Co_2$, $SmFe_{10}CoAl$, and $SmFe_9Co_2Al$. In **a** the nearest- and next-nearest-neighbor exchange interactions of the α-Fe structure are shown in the open circles. Open symbols in **b** and **c** denote the experimental data for $SmFe_{12}$, $SmFe_{11}Ti$, and $SmFe_{9.6}Co_{2.4}$, taken from refs. [15–17,22,23].

One thousand equilibrations, a critical damping of 0.1, and a time step of 1 fs were imposed. The open symbols in Fig. 7b and c denote the available experimental data for $SmFe_{12}$, $SmFe_{11}Ti$, and $SmFe_{9.6}Co_{2.4}$[15–17,22,23]. For both $SmFe_{12}$ and $Sm(Fe,Co)_{12}$, the present theory reproduces the experimental trends of $\mu_0 M_s$ and K_u versus temperature, even though small discrepancies in the absolute values are detected. The main possible causes of such small discrepancies have already been addressed in previous paragraphs. Moreover, the K_u values from the present theory become larger in $SmFe_{10}Co_2$ than in $SmFe_{12}$ at $T > 200$ K, which occurs at a slightly higher temperature of ~300 K in the experiment[22,23]. In our prediction, the room-temperature K_u

values are 7.8 MJ m^{-3} for $SmFe_{10}CoAl$ and 8 MJ m^{-3} for $SmFe_9Co_2Al$ (Fig. 7c).

Table 3 summarizes the present theoretical Curie temperature T_c, anisotropy field $\mu_0 H_a (= 2K_u/M_s)$, and hardness parameter $\kappa (= (K_u/\mu_0 M_s^2)^{1/2})$ at 0, 300, and 500 K in comparison with the available experimental data. We predict T_c to be about 554, 568, 885, 665, and 764 K for $SmFe_{12}$, $SmFe_{11}Ti$, $SmFe_{10}Co_2$, $SmFe_{10}CoAl$, and $SmFe_9Co_2Al$, respectively. The fairly good consistency of the predicted values of $SmFe_{12}$ (554 K), $SmFe_{11}Ti$ (568 K), and $SmFe_{10}Co_2$ (885 K) with the experimental values (555, 597, and 859 K)[22,50,51] conforms the reliability of our calculations. Notably, the T_c (665−764 K) of $Sm(Fe,Co,Al)_{12}$ fulfils the basic requirement of high-performance permanent magnets (i.e., $T_c \geq 550$ K), as suggested in ref. [9]. For $\mu_0 H_a$ and κ, overall the agreement between the present theory and the experiment[22] is satisfactory. In order to further justify a potential replacement of $Sm(Fe,M)_{12}$-based magnets for the currently best permanent magnet $Nd_2Fe_{14}B$, we also compare our results for the present $Sm(Fe,M)_{12}$ systems to the results reported by the previous theoretical and experimental studies for $Nd_2Fe_{14}B$ in Table 3. The obtained results of T_c and $\mu_0 H_a$ as well as κ of the present quaternary $Sm(Fe,Co,Al)_{12}$ systems are superior to the previously reported theoretical (602 K and 2.4−7 T)[30,31] and experimental values (585 K, 4.5−8.8 T, and 1.5)[25–27] of $Nd_2Fe_{14}B$ in the entire temperature range up to 500 K.

Table 3. Predicted Curie temperature T_c (K), anisotropy field $\mu_0 H_a$ (T), and hardness parameter κ of $SmFe_{12}$, $SmFe_{11}Ti$, $SmFe_{10}Co_2$, $SmFe_{10}CoAl$, and $SmFe_9Co_2Al$ at 0, 300, and 500 K.

	T_c	$\mu_0 H_a$			κ		
		0/4.2	300	500	0	300	500
$SmFe_{12}$ (Present theory)	554	19.1	11.5	5.0	2.4	2.1	1.7
$SmFe_{12}$ (Experiment)	555		12.0	2.5		1.7	
$SmFe_{11}Ti$ (Present theory)	568	22.7	14.2	7.3	2.9	2.4	1.6
$SmFe_{11}Ti$ (Experiment)	597		8.3			2.1	
$SmFe_{10}Co_2$ (Present theory)	885	17.4	12.1	9.0	2.3	2.0	1.6
$SmFe_{9.6}Co_{2.4}$ (Experiment)	859		12.0	5.8		1.5	
$SmFe_{10}CoAl$ (Present theory)	665	27.1	18.2	11.3	3.0	2.8	2.5
$SmFe_9Co_2Al$ (Present theory)	764	22.6	14.9	10.2	2.8	2.5	2.2
$Nd_2Fe_{14}B$ (Previous theory)	602		5.4−7.0	2.4−3.5			
$Nd_2Fe_{14}B$ (Experiment)	585	17.0	7.3−8.8	4.5		1.5	

For comparison, we also show the corresponding experimental results for $SmFe_{12}$[22,50,51], $SmFe_{11}Ti$[1,18], $SmFe_{9.6}Co_{2.4}$[22], and $Nd_2Fe_{14}B$[25–27], and the previous theoretical results for $Nd_2Fe_{14}B$[30–31].

Magnetic grain size

The magnetic grain size plays an important role in practice to maximally utilize the intrinsic magnetic properties of a permanent magnet. A permanent magnet exhibits maximal coercivity when the magnet domain grains reach the SD size. Here we estimate the minimal and maximal limits of the stable SD size. The SD size ranges from the minimal stable particle diameter $D_{sp} = (60 k_B T/K_u)^{1/3}$ to the domain threshold diameter $D_{sd} = 72(A_{ex}K_u)^{1/2}/\mu_0 M_s^2$ (A_{ex} is the exchange stiffness constant and $= J_{ex}\langle S^2\rangle/V^{1/3}$)[52,53]. If grain sizes are smaller than D_{sp}, then the particle behaves like a superparamagnet, and if grain sizes are larger than D_{sd}, then the grains are energetically favorable for splitting into multiple domains. The estimated temperature-dependent D_{sp} and D_{sd} are reported in Fig. 8a and b, respectively. For all compounds, both D_{sp} and D_{sd} increase with increasing temperature up to T_c. The increase is primarily a reflection of the reduced $\mu_0 M_s$ and K_u with temperature, as discussed regarding Fig. 7. For $SmFe_{12}$, we find $D_{sp} = 3.5$ nm and $D_{sd} = 48.6$ nm at room temperature. These values at room temperature do not change much upon Co substitution, in reasonable agreement with the experimental SD size of 51 nm in $SmFe_{8.8}Co_{2.2}Ti$[29]. For $SmFe_{10}CoAl$ and $SmFe_9Co_2Al$, $D_{sp} = 3$ and 4.5 nm and $D_{sd} = 90.5$ and 86.3 nm at room temperature, respectively. We note that their stable SD regimes are approximately two times wider than those of the other two compounds ($SmFe_{12}$ and $SmFe_{10}Co_2$) in the entire temperature range up to 500 K.

DISCUSSION

Using systematic DFT, DFPT, and MC simulations, we reveal that the substitutes of simple metal atoms (Ga and Al) for the Fe sites, rather than the conventional TM substitutional elements, stabilize the $ThMn_{12}$-type $Sm(Fe,Co)_{12}$ structure with desirable intrinsic magnetism. In particular, the optimal intrinsic magnetic properties of the quaternary $Sm(Fe,Co,Al)_{12}$ compounds, including the highest K_u of 8 MJ m^{-3}, $\mu_0 H_a$ of 18.2 T, κ of 2.8 at room temperature and a T_c of 764 K, are predicted to be superior to

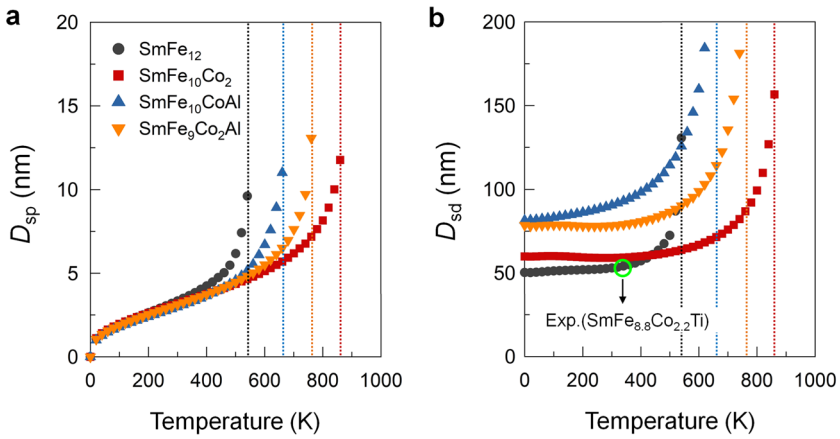

Fig. 8 Temperature-dependent magnetic grain size. a Minimal stable grain size D_{sp} and **b** single-domain threshold size D_{sd} versus temperature of $SmFe_{12}$, $SmFe_{10}Co_2$, $SmFe_{10}CoAl$, and $SmFe_9Co_2Al$. Vertical dotted lines denote the Curie temperatures T_c. Open circle in **b** indicates an experimental single-domain size (51 nm) of $SmFe_{8.8}Co_{2.2}Ti$ at room temperature, taken from ref. [29].

those of the widely investigated $SmFe_{11}Ti$ and $Sm(Fe,Co)_{11}Ti$ magnets, and even to the present ($K_u = 5.4\,MJ\,m^{-3}$) and previously reported theoretical ($4.31\,MJ\,m^{-3}$, $2.4-7.0$ T, and 602 K)[30,31] and experimental results ($4.5\,MJ\,m^{-3}$, 8.8 T, and 1.5 at room temperature and 585 K)[25–27] and for the state-of-the-art magnet $Nd_2Fe_{14}B$. We further predict that the Ga and Al substitutional atoms also significantly improve the SD size of the $Sm(Fe,Co)_{12}$ grains. We hope that the present prediction may resolve the major problem of the structural and thermal instabilities of the $ThMn_{12}$ structure, leading to practical realization of $SmFe_{12}$-based high-performance permanent magnets.

METHODS

We adopted the WIEN2k package[54] with the generalized gradient approximation (GGA) for the exchange-correlation functional[55]. This method accurately deals with both the core and valence electrons and is suitable for *f*-electron magnetic systems. Herein, K_u is defined as $K_u = (E_a - E_c)/volume$, where E_a and E_c are the total energies with magnetization along the *a* and *c* directions, respectively. A total of 1271 *k* points (or a $11 \times 11 \times 21$ *k*-point mesh) were used in the irreducible Brillouin zone[56]. The convergence of K_u with respect to the number of *k* points was seriously checked. The atom-by-atom contribution to E_{MCA} was obtained by switching on/off the SOC of individual atom types in the WIEN2k calculations. The lattice and ionic coordinate relaxations were performed by the Vienna ab initio simulation package (VASP)[57] version 5.4.4. $4s^13d^7$, $4s^13d^8$, and $6s^25p^64f^6$ are treated as valence electrons for Fe, Co, and Sm, respectively. The strongly correlated 4*f* electrons were treated with the Hubbard model in the DFT + U scheme. The effective onsite U_{eff} parameter ($U - J$) was chosen as 6 eV, which is sufficient to split the *f*-orbital bands into lower and upper Hubbard bands[24]. An energy cutoff of 600 eV, a $9 \times 9 \times 17$ *k*-point mesh, and a high force convergence criterion of 10^{-3} eV Å^{-1} were imposed for the structure optimization. The phonon dispersion and thermodynamic properties were carried out by using the PHONOPY code[58] within the harmonic approximation in the DFPT[59] implemented in the VASP. For the phonon calculations, we employed a $2 \times 2 \times 1$ supercell and a $3 \times 3 \times 3$ *k*-point mesh in the interpolation of the force constants matrices. Numerical calculations of temperature-dependent intrinsic magnetic properties and T_c were carried out using MC simulation in the VAMPIRE software package[60,61].

DATA AVAILABILITY

The data that support the findings of this study are available upon reasonable request to the corresponding authors.

Received: 13 November 2021; Accepted: 3 June 2022;
Published online: 09 September 2022

REFERENCES

1. Ohashi, K., Tawara, Y., Osugi, R. & Shimao, M. Magnetic properties of Fe-rich rare-earth intermetallic compounds with a $ThMn_{12}$ structure. *J. Appl. Phys.* **64**, 5714 (1988).
2. Cheng, S. F. et al. Magnetic and structural properties of $SmTiFe_{11-x}Co_x$ alloys. *J. Magn. Magn. Mater.* **75**, 330 (1988).
3. Yang, Y.-C. et al. Magnetic and crystallographic properties of novel Fe-rich rare-earth nitrides of the type $RTiFe_{11}N_{1-\delta}$ (invited). *J. Appl. Phys.* **70**, 6001 (1991).
4. Coehoorn, R. Electronic structure and magnetism of transition-metal-stabilized $YFe_{12-x}M_x$ intermetallic compounds. *Phys. Rev. B* **41**, 11790 (1990).
5. Buschow, K. H. J. *Handbook of Magnetic Materials* Vol. **6** (Elsevier, 1991).
6. Cadieu, F. J., Hegde, H., Navarathna, A., Rani, R. & Chen, K. High-energy product $ThMn_{12}$ Sm-Fe-T and Sm-Fe permanent magnets synthesized as oriented sputtered films. *Appl. Phys. Lett.* **59**, 875 (1991).
7. Buschow, K. H. J. Permanent magnet materials based on tetragonal rare earth compounds of the type $RFe_{12-x}M_x$. *J. Magn. Magn. Mater.* **100**, 79 (1991).
8. Kou, X. C. et al. Magnetic phase transitions, magnetocrystalline anisotropy, and crystal-field interactions in the $RFe_{11}Ti$ series (where R=Y, Pr, Nd, Sm, Gd, Tb, Dy, Ho, Er, or Tm). *Phys. Rev. B* **47**, 3231 (1993).
9. Coey, J. M. D. Permanent magnets: plugging the gap. *Scr. Mater.* **67**, 524 (2012).
10. Skomski, R. & Coey, J. M. D. Magnetic anisotropy – How much is enough for a permanent magnet? *Scr. Mater.* **112**, 3 (2016).
11. Takahashi, Y., Sepehri-Amin, H. & Ohkubo, T. Recent advances in $SmFe_{12}$-based permanent magnets. *Sci. Technol. Adv. Mater.* **22**, 449 (2021).
12. Hirayama, Y., Takahashi, Y. K., Hirosawa, S. & Hono, K. $NdFe_{12}N_x$ hard-magnetic compound with high magnetization and anisotropy field. *Scr. Mater.* **95**, 70 (2015).
13. Sato, T., Ohsuna, T., Yano, M., Kato, A. & Kaneko, Y. Permanent magnetic properties of $NdFe_{12}N_x$ sputtered films epitaxially grown on V buffer layer. *J. Appl. Phys.* **122**, 053903 (2017).
14. Nan-xian, C., Shi-qiang, H., Yu, W. & Jiang, S. Phase stability and site preference of $Sm(Fe,Ti)_{12}$. *J. Magn. Magn. Mater.* **233**, 169 (2001).
15. Hu, B.-P., Li, H.-S., Gavigan, J. P. & Coey, J. M. D. Intrinsic magnetic properties of the iron-rich $ThMn_{12}$-structure alloys $R(Fe_{11}Ti)$; R=Y, Nd, Sm, Gd, Tb, Dy, Ho, Er, Tm and Lu. *J. Phys. Condens. Matter* **1**, 755 (1989).
16. Bodriakov, V. Y., Ivanova, T. I., Nikitin, S. A. & Tereshina, I. S. Magnetic anisotropy and magnetoelastic properties of $SmFe_{11}Ti$. *J. Alloy. Compd.* **259**, 265 (1997).
17. Isnard, O., Guillot, M., Miraglia, S. & Fruchart, D. High field magnetization measurements of $SmFe_{11}Ti$ and $SmFe_{11}TiH_{1-\delta}$. *J. Appl. Phys.* **79**, 5542 (1996).
18. Harashima, Y., Terakura, K., Kino, H., Ishibashi, S. & Miyake, T. First-principles study of structural and magnetic properties of $R(Fe,Ti)_{12}$ and $R(Fe,Ti)_{12}N$ (R=Nd,Sm,Y). *Proc. Comput. Sci. Workshop* **5**, 011021 (2015).
19. Harashima, Y., Terakura, K., Kino, H., Ishibashi, S. & Miyake, T. First-principles study on stability and magnetism of $NdFe_{11}M$ and $NdFe_{11}MN$ for M=Ti, V, Cr, Mn, Fe, Co, Ni, Cu, Zn. *J. Appl. Phys.* **120**, 203904 (2016).
20. De Boer, F. R., Yung-Kai, H., De Mooij, D. B. & Buschow, K. H. J. Magnetic properties of a series of novel ternary intermetallics ($RFe_{10}V_2$). *J. Less. Common. Met.* **135**, 199 (1987).
21. Schönhöbel, A. M. et al. Intrinsic magnetic properties of $SmFe_{12-x}V_x$ alloys with reduced V-concentration. *J. Alloy. Compd.* **786**, 969 (2019).
22. Hirayama, Y., Takahashi, Y. K., Hirosawa, S. & Hono, K. Intrinsic hard magnetic properties of $Sm(Fe_{1-x}Co_x)_{12}$ compound with the $ThMn_{12}$ structure. *Scr. Mater.* **138**, 62 (2017).
23. Ogawa, D. et al. Magnetic anisotropy constants of $ThMn_{12}$-type $Sm(Fe_{1-x}Co_x)_{12}$ compounds and their temperature dependence. *J. Magn. Magn. Mater.* **497**, 165965 (2020).
24. Odkhuu, D., Ochirkhuyag, T. & Hong, S. C. Enhancing energy product and thermal stability of $SmFe_{12}$ by interstitial doping. *Phys. Rev. Appl.* **13**, 054076 (2020).
25. Durst, K.-D. & Kronmuller, H. Determination of intrinsic magnetic material parameters of $Nd_2Fe_{14}B$ from magnetic measurements of sintered $Nd_{15}Fe_{77}B_8$ magnets. *J. Magn. Magn. Mater.* **59**, 86 (1986).
26. Yamamoto, H., Matsuura, Y., Fujimura, S. & Sagawa, M. Magnetocrystalline anisotropy of $R_2Fe_{14}B$ tetragonal compounds. *Appl. Phys. Lett.* **45**, 1141 (1984).
27. Herbst, J. F. $R_2Fe_{14}B$ materials: Intrinsic properties and technological aspects. *Rev. Mod. Phys.* **63**, 819 (1991).
28. Sun, H., Otani, Y., Coey, J. M. D., Meekison, C. D. & Jakubovics, J. P. Coercivity and microstructure of melt-spun $Sm(Fe_{11}Ti)$. *J. Appl. Phys.* **67**, 4659 (1990).
29. Qian, H.-D. et al. Phase transformation and magnetic properties of fully dense $Sm(Fe_{0.8}Co_{0.2})_{11}Ti$ bulk magnets. *Scr. Mater.* **193**, 17 (2021).
30. Sepehri-Amin, H., Ohkubo, T. & Hono, K. Micromagnetic simulations of magnetization reversals in Nd-Fe-B based permanent magnets. *Mater. Trans.* **57**, 1221 (2016).
31. Gong, Q., Yi, M., Evans, R. F. L., Xu, B.-X. & Gutfleisch, O. Calculating temperature-dependent properties of $Nd_2Fe_{14}B$ permanent magnets by atomistic spin model simulations. *Phys. Rev. B* **99**, 214409 (2019).
32. Delange, P., Biermann, S., Miyake, T. & Pourovskii, L. Crystal-field splittings in rare-earth-based hard magnets: an ab initio approach. *Phys. Rev. B* **96**, 155132 (2017).
33. Dirba, I. et al. Thermal decomposition of $ThMn_{12}$-type phase and its optimum stabilizing elements in $SmFe_{12}$-based alloys. *J. Alloy. Compd.* **813**, 152224 (2020).
34. Saengdeejing, A. & Chen, Y. Improving thermodynamic stability of $SmFe_{12}$-type permanent magnets from high entropy effect. *J. Phase. Equilib. Diffus.* **42**, 592 (2021).
35. Jain, A. The Materials Project: A materials genome approach to accelerating materials innovation. *APL Mater.* **1**, 011002 (2013).
36. Barber, C. B., Dobkin, D. P. & Huhdanpaa, H. The quickhull algorithm for convex hulls. *ACM Trans. Math. Softw.* **22**, 469 (1996).
37. Akbarzadeh, A. R., Ozolins, V. & Wolverton, C. First-principles determination of multicomponent hydride phase diagrams: application to the Li-Mg-N-H system. *Adv. Mater.* **19**, 3233 (2007).
38. Emery, A. A. & Wolverton, C. High-throughput DFT calculations of formation energy, stability and oxygen vacancy formation energy of ABO_3 perovskites. *Sci. Data* **4**, 170153 (2017).
39. Suski, W. *Handbook on the Physics and Chemistry of Rare Earth* Vol. **22** (North-Holland Physics Publishing, 1996).
40. Miyake, T. & Akai, H. Quantum theory of rare-earth magnets. *J. Phys. Soc. Jpn.* **87**, 041009 (2018).
41. Bronova, A., Bredow, T., Glaum, R., Riley, M. J. & Urland, W. BonnMag: Computer program for ligand-field analysis of f^n systems within the angular overlap model. *J. Comp. Chem.* **39**, 176 (2018).

42. Bruno, P. Tight-binding approach to the orbital magnetic moment and magnetocrystalline anisotropy of transition-metal monolayers. *Phys. Rev. B* **39**, 865(R) (1989).
43. Sözen, H. I. et al. Ab initio phase stabilities of Ce-based hard magnetic materials and comparison with experimental phase diagrams. *Phys. Rev. Mater.* **3**, 084407 (2019).
44. Mediukh, N. R., Ivashchenko, V. I., Pogrebnjak, D. A. & Shevchenko, V. I. First-principles study of thermodynamic and stability properties of TiC-SiC alloys. *Proc. NAP* **1**, 01NTF4 (2019).
45. Novak, P. & Rusz, J. Exchange interactions in barium hexaferrite. *Phys. Rev. B* **71**, 184433 (2005).
46. Odkhuu, D. & Hong, S. C. First-principles prediction of possible rare-earth free permanent magnet of tetragonal FeCo with enhanced magnetic anisotropy and energy product through interstitial nitrogen. *Phys. Rev. Appl.* **11**, 054085 (2019).
47. Odkhuu, D. & Hong, S. C. Simultaneous tuning of the magnetic anisotropy and thermal stability of α''-phase $Fe_{16}N_2$. *Sci. Rep.* **11**, 7823 (2021).
48. Schilfgaarde, M. V. & Antropov, V. P. First-principles exchange interactions in Fe, Ni, and Co. *J. Appl. Phys.* **85**, 4827 (1999).
49. Lezaic, M., Mavropoulos, P. & Blügel, S. First-principles prediction of high Curie temperature for ferromagnetic bcc-Co and bcc-FeCo alloys and its relevance to tunneling magnetoresistance. *Appl. Phys. Lett.* **90**, 082504 (2007).
50. Wang, D. et al. $SmFe_{12}$ and $SmFe_{12}N_x$ films fabricated by sputtering. *J. Magn. Magn. Mater.* **124**, 62 (1993).
51. Sun, H., Tomida, T. & Hirosawa, S. Magnetic properties and microstructure studies of Sm-Fe magnetic thin films. *J. Appl. Phys.* **81**, 328 (1997).
52. Bruck, E. *Handbook of Magnetic Materials* Vol. **1**, (Elsevier, 2018).
53. Charap, S. H., Lu, P. L. & He, Y. Thermal stability of recorded information at high densities. *IEEE Trans. Magn.* **33**, 978 (1997).
54. Blaha, P., Schwarz, K., Madsen, G. K. H., Kvasnicka, D. & Luitz, J. *WIEN2k, An augmented plane wave + Local orbitals program for calculating crystal properties*. (Technische Universitat Wien, 2001).
55. Perdew, J. P. et al. Atoms, molecules, solids, and surfaces: Applications of the generalized gradient approximation for exchange and correlation. *Phys. Rev. B* **46**, 6671 (1992).
56. Monkhorst, H. J. & Pack, J. D. Special points for Brillouin-zone integrations. *Phys. Rev. B* **13**, 5188 (1976).
57. Kresse, G. & Hafner, J. Ab initio molecular dynamics for liquid metals. *Phys. Rev. B* **47**, 558(R) (1993).
58. Togo, A. & Tanaka, I. First principles phonon calculations in materials science. *Scr. Mater.* **108**, 1 (2015).
59. Giannozzi, P., Gironcoli, S., Pavone, P. & Baroni, S. Ab initio calculation of phonon dispersions in semiconductors. *Phys. Rev. B* **43**, 7231 (1991).
60. Asselin, P. et al. Constrained Monte Carlo method and calculation of the temperature dependence of magnetic anisotropy. *Phys. Rev. B* **82**, 054415 (2010).
61. Metropolis, N., Rosenbluth, A. W., Rosenbluth, M. N., Teller, A. H. & Teller, E. Equations of state calculations by fast computing machines. *J. Chem. Phys.* **21**, 1087 (1953).

ACKNOWLEDGEMENTS

This work is supported by the Future Materials Discovery Program (Grant No. 2016M3D1A1027831) and the Basic Research Program (Grant No. 2020R1F1A1067589) through the National Research Foundation of Korea (NRF) funded by the Ministry of Science and ICT and the Korea Institute of Energy Technology Evaluation and Planning (KETEP) grant funded by the Korea government (MOTIE) (Grant No. 20192010106850, Development of magnetic materials for IE4 class motor).

AUTHOR CONTRIBUTIONS

S.C.H. and D.O. conceived the project and wrote the paper. T.O. performed the calculations. All authors reviewed the paper.

COMPETING INTERESTS

The authors declare no competing interests.

ADDITIONAL INFORMATION

Correspondence and requests for materials should be addressed to Soon Cheol Hong or Dorj Odkhuu.

Reprints and permission information is available at http://www.nature.com/reprints

Publisher's note Springer Nature remains neutral with regard to jurisdictional claims in published maps and institutional affiliations.

Open Access This article is licensed under a Creative Commons Attribution 4.0 International License, which permits use, sharing, adaptation, distribution and reproduction in any medium or format, as long as you give appropriate credit to the original author(s) and the source, provide a link to the Creative Commons license, and indicate if changes were made. The images or other third party material in this article are included in the article's Creative Commons license, unless indicated otherwise in a credit line to the material. If material is not included in the article's Creative Commons license and your intended use is not permitted by statutory regulation or exceeds the permitted use, you will need to obtain permission directly from the copyright holder. To view a copy of this license, visit http://creativecommons.org/licenses/by/4.0/.

© The Author(s) 2022